Eur. Phys. J. A (2016) **52**: 60
DOI 10.1140/epja/i2016-16060-y

THE EUROPEAN PHYSICAL JOURNAL A

Regular Article – Theoretical Physics

Hybrid star structure with the Field Correlator Method*

G.F. Burgio[a] and D. Zappalà

INFN, Sezione di Catania, Via Santa Sofia 64, 95123 Catania, Italy

Received: 28 July 2015 / Revised: 17 December 2015
Published online: 22 March 2016 – © Società Italiana di Fisica / Springer-Verlag 2016
Communicated by D. Blaschke

Abstract. We explore the relevance of the color-flavor locking phase in the equation of state (EoS) built with the Field Correlator Method (FCM) for the description of the quark matter core of hybrid stars. For the hadronic phase, we use the microscopic Brueckner-Hartree-Fock (BHF) many-body theory, and its relativistic counterpart, *i.e.* the Dirac-Brueckner (DBHF). We find that the main features of the phase transition are directly related to the values of the quark-antiquark potential V_1, the gluon condensate G_2 and the color-flavor superconducting gap Δ. We confirm that the mapping between the FCM and the CSS (constant speed of sound) parameterization holds true even in the case of paired quark matter. The inclusion of hyperons in the hadronic phase and its effect on the mass-radius relation of hybrid stars is also investigated.

1 Introduction

The possible appearance of quark matter (QM) in the interior of massive neutron stars (NS) is currently one of the main theoretical issues in the physics of compact stars [1]. The existence of two NS of about two solar masses has been confirmed by recent observations [2,3]. Based on a microscopic nucleonic equation of state (EoS), one expects that in such heavy NS the central particle density reaches values larger than $1/\mathrm{fm}^3$, where in fact quark degrees of freedom are expected to appear at a macroscopic level. Unfortunately, while the microscopic theory of the nucleonic EoS has reached a high degree of sophistication [4–8], the QM EoS is still poorly known at zero temperature and at the high baryonic density appropriate for NS. In fact the essential theoretical tool, *i.e.* lattice formulation of the quantum chromodynamics (QCD) is inapplicable at large baryon densities and small temperature due to the so-called Sign Problem [9], and this is due to its complicated nonlinear and nonperturbative nature. On the other hand, in the large temperature and small density region lattice QCD simulations have provided controlled results for the EoS as well as for the nature of the transition [10,11].

The mass of a NS can be calculated by solving the Tolman-Oppenheimer-Volkoff (TOV) equations with the relevant EoS as input. The hybrid EoS including both hadronic matter and QM is usually obtained by combining EoSs of hadronic matter and QM within individual theories/models.

Continuing a set of investigations using different quark models [12–16], recently we have explored the nature of the phase transition with the Field Correlator Method (FCM) model of quark matter [17–19], which in principle is able to cover the full temperature-chemical potential plane. In our previous papers [20,21], we tested the FCM model by comparing the results for the neutron star masses with the existing phenomenology, which puts strong constraints on the parameters of the model, *i.e.* the quark-antiquark potential V_1 and the gluon condensate G_2.

Recently, we found that the FCM model can be expressed in the language of the "Constant Speed of Sound" (CSS) parameterization [22,23], and we showed how its parameters can be mapped on to the CSS parameter space. We remind that the CSS scheme is a general parameterization suitable for expressing experimental constraints in a model-independent way, and for classifying different models of quark matter and establishing connections among them. It is applicable to high-density equations of state for which: a) there is a sharp interface between nuclear matter and quark matter, b) the speed of sound in the high-density matter is pressure-independent in the range between the first-order transition pressure up to the maximum central pressure of neutron stars. Given the nuclear matter EoS $\epsilon_{\mathrm{NM}}(p)$, the high-density EoS can be expressed as

$$\epsilon(p) = \begin{cases} \epsilon_{\mathrm{NM}}(p), & p < p_{\mathrm{trans}}, \\ \epsilon_{\mathrm{NM}}(p_{\mathrm{trans}}) + \Delta\epsilon + c_{\mathrm{QM}}^{-2}(p - p_{\mathrm{trans}}), & p > p_{\mathrm{trans}}, \end{cases} \tag{1}$$

where the three parameters: the pressure p_{trans} at the transition, the discontinuity in energy density $\Delta\epsilon$ at the

* Contribution to the Topical Issue on "Exotic matter in neutron stars" edited by David Blaschke, Jürgen Schaffner-Bielich, Hans-Josef Schulze.

[a] e-mail: fiorella.burgio@ct.infn.it

transition, and the speed of sound $c_{\rm QM}$ characterize completely the high-density phase.

In this work we elaborate more on that point by extending the FCM model in order to include the color superconductivity through the color-flavor locking (CFL) mechanism, which mimics an explicit dependence of the gluon condensate G_2 on the quark chemical potential, as initially studied in ref. [21]. We find that the value of the hybrid star maximum mass depends strongly on the FCM model parameters, *i.e.* V_1, G_2 and the gap Δ. We also find that the mapping on to the CSS parameterization still holds true when including the CFL phase, though the parameter region explored depends on the value of the gap Δ. We also pay special attention to the analysis of the hadron-quark phase transition when hyperons are included in the hadronic phase. In fact, given the strong softening of the EoS due to hyperons, it has been often found that no quark matter phase transition can take place [13, 16].

This paper is organized as follows. In the next section we briefly review the EoS of the hadronic sector, particularly the BHF and DBHF microscopic approaches. In sect. 3 we discuss the quark matter EoS, and in sect. 3.1 we illustrate the FCM at finite density, with the inclusion of the color-flavor locking effect in sect. 3.2. Section 4 contains numerical results, with some details of the EoS for neutron star matter and the hadron-quark phase transition in sect. 4.1. In sect. 4.2 we discuss the mass-radius-central density relation for hybrid stars, and the FCM mapping onto the CSS parameterization. Effects due to the inclusion of hyperons are explored in sect. 4.3. Finally we draw our conclusions in sect. 5.

2 The BHF and DBHF EoS of nuclear matter

Empirical properties of infinite nuclear matter can be calculated using many different theoretical approaches. The amount of experimental and observational data obtained in the last few years, and the intense theoretical efforts aimed at their interpretation, call for a firm microscopic approach to the modeling of the Equation of State (EoS). In a microscopic approach, the only input required is a realistic free nucleon-nucleon (NN) interaction with parameters fitted to NN scattering phase shifts in different partial wave channels, and to properties of the deuteron. In this paper we adopt the nonrelativistic Brueckner-Bethe-Goldstone (BBG) method [24] and its relativistic counterpart, the Dirac-Brueckner-Hartree-Fock (DBHF) approximation [25].

The Brueckner-Bethe-Goldstone (BBG) theory is based on a linked cluster expansion of the energy per nucleon of nuclear matter (see ref. [24], chapter 1 and references therein). The basic ingredient in this many-body approach is the Brueckner reaction matrix G, which is the solution of the Bethe-Goldstone equation

$$G[\rho;\omega] = v + \sum_{k_a k_b} v \frac{|k_a k_b\rangle Q \langle k_a k_b|}{\omega - e(k_a) - e(k_b)} G[\rho;\omega], \qquad (2)$$

where v is the bare NN interaction, ρ is the nucleon number density, and ω the starting energy. The single-particle energy $e(k)$ (assuming $\hbar = 1$),

$$e(k) = e(k;\rho) = \frac{k^2}{2m} + U(k;\rho), \qquad (3)$$

and the Pauli operator Q determine the propagation of intermediate baryon pairs. The Brueckner-Hartree-Fock (BHF) approximation for the single-particle potential U using the *continuous choice* is

$$U(k;\rho) = \sum_{k' \le k_F} \langle kk'|G[\rho; e(k) + e(k')]|kk'\rangle_a, \qquad (4)$$

where the subscript "a" indicates antisymmetrization of the matrix element. Due to the occurrence of $U(k)$ in eq. (3), the above equations constitute a coupled system that has to be solved in a self-consistent manner for several momenta of the particles involved, at the considered densities. In the BHF approximation the energy per nucleon is

$$\frac{E}{A} = \frac{3}{5}\frac{k_F^2}{2m} + \frac{1}{2\rho} \sum_{k,k' \le k_F} \langle kk'|G[\rho; e(k) + e(k')]|kk'\rangle_a. \qquad (5)$$

In this scheme, the only input quantity we need is the bare NN interaction v in the Bethe-Goldstone equation (1). It has been shown that the nuclear EoS can be calculated with good accuracy in the Brueckner two hole-line approximation with the continuous choice for the single-particle potential, since the results in this scheme are quite close to the calculations which include also the three hole-line contribution [26–28]. The dependence on the NN interaction, also within other many-body approaches, has been systematically investigated in ref. [7].

However, it is commonly known that nonrelativistic calculations, based on purely two-body interactions, do not reproduce correctly the saturation point of symmetric nuclear matter, and that three-body forces (TBF) are needed to correct this deficiency. For that, TBF are reduced to a density dependent two-body force by averaging over the generalized coordinates (position, spin and isospin) of the third particle, assuming that the probability of having two particles at a given distance is reduced according to the two-body correlation function [4, 6, 29].

In this work we will illustrate results obtained using a phenomenological approach to the TBF, which is based on the so-called Urbana model, and consists of an attractive term due to two-pion exchange with excitation of an intermediate Δ resonance, and a repulsive phenomenological central term [30, 31]. Within the BHF approach, those TBF produce a shift of about $+1$ MeV in energy and $-0.1\,\mathrm{fm}^{-3}$ in density. This adjustment is obtained by tuning the two parameters contained in the TBF, and is performed to get an optimal saturation point [4, 6].

Besides a purely phenomenological model, microscopic TBF have also been derived and a tentative approach proposed using the same meson-exchange parameters as the underlying NN potential. Results have been obtained with

the Argonne v_{18}, the Bonn B, and the Nijmegen 93 potentials [8, 32]. However, at present the theoretical status of microscopically derived TBF is still quite rudimentary, Alternatively, latest nuclear matter calculations [33, 34] used a new class of chiral inspired TBF [35–37], showing that the considered TBF models are not able to reproduce simultaneously the correct saturation point and the properties of three- and four-nucleon systems.

Recently, it has been shown that the role of TBF is greatly reduced if the NN potential is based on a realistic constituent quark model [38, 39] which can explain at the same time few-nucleon systems and nuclear matter, including the observational data on Neutron Stars and the experimental data on heavy-ions collisions. Moreover it has been found that at the highest densities the three-hole-line diagrams can give a contribution larger than the two-hole-line diagrams, and this can be related to the characteristic nonlocality of the repulsive core [40] as produced by the quark-exchange processes.

In the past years, the BHF approach has been extended in order to include the hyperon degrees of freedom [41, 42], which play an important role in the study of neutron star matter. In fact, hyperons are expected to appear in beta-stable matter already at relatively low densities of about twice nuclear saturation density, thus producing a softening of the EoS with a strong decrease of the maximum mass. If this is the case, the existence of heavy NS would question the presence of hyperons in their interior, thus requiring alternative scenarios. It is therefore of great importance to carry out accurate theoretical calculations of hypernuclear matter starting from the available information on both nucleon and hyperon interactions. There exist several hyperon-nucleon (NY) potentials fitted to scattering data, *i.e.* NSC89 [43], NSC97 [44], and ESC08 [45], while the hyperon-hyperon (YY) potentials have presently to be considered rather uncertain or unknown, which is basically due to the lack of appropriate experimental data. An alternative description of the hyperon-nucleon system has been recently achieved at next-to-leading order in chiral effective field theory [46, 47].

In the Brueckner scheme, we have used the phenomenological NY potentials [43–45] as fundamental input, and found very low maximum masses of hyperon stars, below $1.4M_\odot$ ($M_\odot = 2 \times 10^{33}$ g). A proposed solution of this so-called *hyperon puzzle* focuses on the role played by hyperonic three-body forces, and several attempts have been made in this direction [48–51]. However, many inconsistencies still remain, and the solution to this problem is still far from being understood.

The relativistic framework is the one on which the nuclear EoS should be ultimately based. The best relativistic treatment developed so far is the Dirac-Brueckner (DBHF) approach [25]. The DBHF method can be developed in analogy with the nonrelativistic case, *i.e.* the nucleon inside the nuclear medium is viewed as a dressed particle in consequence of its two-body interaction with the surrounding nucleons. The two-body correlations are described by introducing the in-medium relativistic G-matrix. The DBHF scheme can be formulated as a self-consistent problem between the single particle self-energy Σ and the G-matrix. It has been shown that the DBHF treatment is equivalent [52] to introducing in the nonrelativistic BHF the three-body force corresponding to the excitation of a nucleon-antinucleon pair, the so-called Z-diagram [53], which is repulsive at all densities, and consequently produces a saturating effect. Actually, including in BHF only these particular TBF, one gets results close to DBHF calculations, see ref. [54]. Generally speaking, the DBHF gives in general a better saturation point than BHF, and the corresponding EoS turns out to be stiffer above saturation than the one calculated from the BHF + TBF method. In the relativistic context the only NN potentials which have been developed are the ones of one-boson exchange type. In the calculations shown here the Bonn A potential is used [25]. Recently, the properties of neutron-star matter including hyperons have been investigated within the DBHF approach [55]. In the calculation, the effect of negative-energy states of baryons was partly taken into account, as well as both time and space components of the vector self-energies of baryons and the scalar ones. A value of $2.08M_\odot$ was obtained for the maximum neutron-star mass, consistent with the recently observed, massive neutron stars [2, 3].

3 The quark matter EoS

3.1 The Field Correlator Method

The approach we follow to describe the quark matter EoS was introduced in [17–19]; see ref. [56] for a review. For our purposes, we are specifically interested in the extension of this approach to finite baryon density and temperature, and all we need is the expression of the pressure as a function of the EoS thermodynamical parameters, *i.e.* the baryon chemical potential μ_B and the temperature T. This is derived in [57–59], and below we report its explicit form. The full pressure, P_{qg}, is the sum of the gluon, P_g, the quark, P_q, and the vacuum, P_v, contributions

$$P_{qg} = P_g + \sum_{j=u,d,s} P_q^j + P_v, \tag{6}$$

where the sum is extended to the three light quark flavors. The gluon pressure is

$$P_g = \frac{8T^4}{3\pi^2} \int_0^\infty \mathrm{d}\chi \chi^3 \frac{1}{\exp(\chi + \frac{9V_1}{8T}) - 1}\,, \tag{7}$$

while the quark pressure for each single flavor with mass m_q and chemical potential μ_q, is

$$P_q = \frac{T^4}{\pi^2} \left[\phi_\nu \left(\frac{\mu_q - V_1/2}{T} \right) + \phi_\nu \left(-\frac{\mu_q + V_1/2}{T} \right) \right], \tag{8}$$

where

$$\phi_\nu(a) = \int_0^\infty \mathrm{d}u \frac{u^4}{\sqrt{u^2+\nu^2}} \frac{1}{(\exp[\sqrt{u^2+\nu^2} - a] + 1)}\,, \tag{9}$$

being $\nu = m_q/T$. Finally P_v, which represents the pressure difference between the vacua in the deconfined and confined phases, is given by

$$P_v = -\frac{(11 - \frac{2}{3}N_f)}{32}\frac{G_2}{2}\,, \tag{10}$$

where the number of light flavors in our case is $N_f = 3$.

Then, once the quark chemical potentials are related to the baryon chemical potential μ_B, the full pressure P_{qg} is defined in terms of the two parameters V_1 and G_2 appearing in eqs. (7)–(10), where V_1 indicates the large distance static $q\bar{q}$ potential and G_2 is the gluon condensate. The former is essentially of nonperturbative nature and can be expressed in terms of an integral of a fundamental QCD correlator [57–59]; however there is no direct measurement of its value. The latter is known from QCD sum rules [60, 61], $G_2 = \langle \frac{\alpha_s}{\pi} G^a_{\mu\nu} G^{a\,\mu\nu} \rangle = 0.012\,\mathrm{GeV}^4$, although an uncertainty of about 50% affects this estimate.

It is also interesting to notice that G_2 appears only in the vacuum contribution to the pressure, and P_v in eq. (10) has the same role of the bag constant of the MIT bag model. Moreover, if one turns off the potential V_1, the quark pressure P_q becomes the pressure of free quarks, and in this case the FCM model reduces to the simplest version of the bag model. Therefore V_1 can be regarded as the main correction to the free quarks dynamics inside the bag.

In addition to the poor knowledge of the phenomenological values of V_1 and G_2, one has also to deal with the dependence of these parameters on the thermodynamical variables μ_B and T. In fact, for the T dependence some indications can be obtained from the analysis of the deconfinement phase transition at $T = T_c$ and $\mu_B = 0$, which is supported by lattice calculations. For instance, the fact that the gluon condensate G_2 is substantially T independent except at T_c, where it is sharply reduced by one half [62, 63], was already accounted for in the vacuum pressure difference of the two phases derived in [57] and reported in eq. (10).

As far as V_1 is concerning, the following expression relating $V_1(T_c)$, G_2 and T_c is derived within the FCM model, in [57, 58],

$$T_c = \frac{a_0 G_2^{1/4}}{2}\left(1 + \sqrt{1 + \frac{V_1(T_c)}{2a_0 G_2^{1/4}}}\right), \tag{11}$$

being $a_0 = (3\pi^2/768)^{1/4}$. Then, in [64] it is shown that, with $G_2 = 0.012\,\mathrm{GeV}^4$ and with the lattice estimates of the critical temperature, $T_c = 147 \pm 5\,\mathrm{MeV}$ or $T_c = 154 \pm 9\,\mathrm{MeV}$, eq. (11) yields $V_1(T_c) \lesssim 0.15\,\mathrm{GeV}$. Another analysis, [21], based on a fit to the lattice determination of the interaction measure $(\epsilon - 3p)/T^4$ at several values of the temperature around and above T_c, suggests a larger potential, $V_1(T_c) \sim 0.5$–$0.6\,\mathrm{GeV}$, which, according to eq. (11) computed at these T_c, requires a smaller gluon condensate, $G_2 \simeq 0.003$–$0.004\,\mathrm{GeV}^4$. In addition to these estimates, an analytic expression for $V_1(T)$, which allows to relate $V_1(T_c)$ to the value of the potential at zero temperature, $V_1(T = 0)$, was derived within the FCM in [64] and, in particular, it turns out that $V_1(T_c) \sim 0.5$–$0.6\,\mathrm{GeV}$ corresponds to $V_1(T = 0) \simeq 0.8$–$0.9\,\mathrm{GeV}$.

At this point, it is essential to recall that all these results are obtained at zero baryon density while, in the core of NS, densities as large as many times the nuclear matter saturation density and low temperatures are expected. Unfortunately, no lattice simulation can be performed in QCD at high μ_B, and therefore no numerical indication on the density dependence of the two parameters of the FCM is available. On the other hand, in the extension of the FCM at finite chemical potential discussed in [58], the authors claim that the potential V_1 is expected to be independent of μ_B at least for small values of μ_B. However this statement cannot be straightforwardly extended to the region of very large density where the environment is strongly modified: the number of antiparticles becomes much smaller than the number of particles. Therefore, even if the interaction strength of quark-antiquark pairs is larger than that of quark-quark pairs, the latter plays a more important role because of the dominance of quarks over antiquarks. In addition, within this framework the particle pairing can lead to the appearance of new phases that will be discussed in sect. 3.2.

In view of all the above considerations, it is evident that we have very few indications on V_1 at large baryon density and low temperature, and therefore the best strategy is to treat it as a free parameter of the FCM, with no *a priori* assumed dependence on T or μ_B, which effectively measures the large distance interaction strength within a finite quark density environment, and which has to be constrained by the observational data on heaviest NS, through our analysis. Accordingly, we do not try to relate $V_1(\mu_B)$ to $V_1(\mu_B = 0)$ and in particular to those values of V_1 at deconfinement transition, quoted above. Therefore, the widest acceptable range of V_1 is explored: so, for instance, even the case $V_1 < 0$ is examined, although, as we shall see below, it does not produce sufficiently heavy hybrid NS. Finally, as explained more in detail in sect. 3.2, the other parameter of the FCM, G_2, is also treated a free parameter in our analysis, essentially for the same reasons discussed in the case of V_1.

3.2 The color-flavor locking effect

In ref. [21] the dependence of G_2 on μ_B was explicitly studied by introducing a particular ansatz for $G_2(\mu_B)$, which was based on previous analysis of the expectation of the gluon condensate in dense nuclear matter [65–67] and in two-color, $N_c = 2$, quantum chromodynamics [68, 69]. In particular, in [68, 69] it is shown that the explicit form obtained for $G_2(\mu_B)$ (it starts as a decreasing function at small μ_B and turns into an increasing function at larger μ_B, with a minimum between these two regions) is related to the effect of diquark pairing and the appearance of a mass gap. In fact, at a qualitative level this effect presents strong similarities with the occurrence of the color-flavor locking (CFL) superconductive mechanism in standard $N_c = 3$ QCD [70, 71], which, as far as the total pressure of the quark system is concerned, induces an additional

pressure term parameterized by a gap Δ. Clearly, this new pressure term has an essential role in shaping the μ_B dependence of the gluon condensate G_2, which eventually has the same qualitative features of the curve derived in [69].

Therefore, due to the unavoidable arbitrariness associated to the choice of the ansatz for $G_2(\mu_B)$ encountered in [21], rather than following that approach we prefer to adopt here the same point of view taken for the other FCM parameter V_1, *i.e.* we take G_2 as a free parameter independent of T and μ_B, that sets the pressure and the energy density of the vacuum. Then, the FCM described by the two free parameters V_1 and G_2, is suitable to study the high density region, and the possible additional contribution due to the new CFL phase, associated to quark-quark pairing, has to be taken into account by adding the additional CFL pressure contribution to the full FCM pressure P_{qg}.

The presence of color-flavor locked quark matter is expected at very high μ_B, and it is realized through quark-quark pairing under the constraint that the densities of the three flavors, up, down and strange, are equal [71–74]. The global effect of this pairing on the pressure is the presence of the additional term

$$P_{cfl} = \frac{\Delta^2 \mu_B^2}{3\pi^2}\,, \tag{12}$$

only when the chemical potential is greater than $\mu_B = 3m_s^2/(4\Delta)$ and the gap Δ is expected to be in the range 10–100 MeV in the region of interest of μ_B for the NS. Finally the total pressure of the quark matter phase is obtained by adding P_{cfl} to P_{qg} given in eq. (6), and is treated as a function of the baryon chemical potential μ_B with three free parameters, namely the potential V_1 and the gluon condensate G_2, coming from the FCM model, and the gap Δ, due to the CFL pairing.

4 Numerical results

4.1 EoS of dense matter in beta equilibrium

In order to study the structure of NS, we have to calculate the composition and the EoS of cold, neutrino-free, charge-neutral, and beta-stable matter, characterized by two degrees of freedom μ_B and μ_e, the baryon and charge chemical potentials. The corresponding equations are

$$\mu_i = b_i\mu_B - q_i\mu_e, \qquad \sum_i \rho_i q_i = 0, \tag{13}$$

b_i and q_i denoting baryon number and charge of the particle species $i = n, p, e, \mu$ in the hadron phase and $i = u, d, s, e, \mu$ in the quark phase, respectively.

As far as the hadronic phase is concerning, the Brueckner calculation yields the energy density of baryon/lepton matter as a function of the different partial densities,

$$\epsilon(\rho_n,\rho_p,\rho_e,\rho_\mu) = (\rho_n m_n + \rho_p m_p) + (\rho_n+\rho_p)\frac{E}{A}(\rho_n,\rho_p) + \epsilon_\mu(\rho_\mu) + \epsilon_{el}(\rho_{el}), \tag{14}$$

where we have used relativistic and ultrarelativistic approximations for the energy densities of muons and electrons, respectively [75]. In practice, it is sufficient to compute only the binding energy of symmetric nuclear matter and pure neutron matter, since within the BHF approach it has been verified [4,76] that a parabolic approximation for the binding energy of nuclear matter with arbitrary proton fraction $x = \rho_p/\rho$, $\rho = \rho_n + \rho_p$, is well fulfilled,

$$\frac{E}{A}(\rho,x) \approx \frac{E}{A}(\rho, x=0.5) + (1-2x)^2 E_{\rm sym}(\rho), \tag{15}$$

where the symmetry energy $E_{\rm sym}$ can be expressed in terms of the difference of the energy per particle between pure neutron ($x = 0$) and symmetric ($x = 0.5$) matter:

$$E_{\rm sym}(\rho) = \frac{1}{8}\frac{\partial^2(E/A)}{\partial x^2}\bigg|_{x=0.5} \approx \frac{E}{A}(\rho,0) - \frac{E}{A}(\rho,0.5). \tag{16}$$

Once the energy density is known (eq. (14)), the various chemical potentials (of the species $i = n, p, e, \mu$) can be computed straightforwardly,

$$\mu_i = \frac{\partial\epsilon}{\partial\rho_i}\,, \tag{17}$$

and the equations for beta-equilibrium (13) allow one to determine the equilibrium composition $\{\rho_i\}$ at given baryon density ρ and finally the EoS,

$$P = \rho^2\frac{\mathrm{d}}{\mathrm{d}\rho}\frac{\epsilon(\{\rho_i(\rho)\})}{\rho} = \rho\frac{\mathrm{d}\epsilon}{\mathrm{d}\rho} - \epsilon = \rho\mu_B - \epsilon. \tag{18}$$

As far as the quark phase is concerned, it is necessary to define the relations among the various μ_q that appear in eq. (8) and the variable μ_B. For this purpose we must distinguish two cases, one with $\Delta = 0$ and the other with $\Delta \neq 0$. In the first case one has $P_{cfl} = 0$ and the corresponding EoS for quark matter is determined by the conditions of β-equilibrium and charge neutrality and baryon number conservation, as expressed by eq. (13). It is then sufficient to express each μ_q in terms of one single variable, namely μ_B. In the second case, with $\Delta \neq 0$, the charge neutrality condition is realized in a peculiar way [72]. In fact, CFL pairing occurs if the number densities of the three flavors are equal

$$\rho_u = \rho_d = \rho_s, \tag{19}$$

which implies vanishing electron density, $\rho_e = 0$, in order to maintain full charge neutrality. As explained in [72], eqs. (19) with nonvanishing strange quark mass, $m_s \neq 0$, are acceptable only if $\mu_e \neq 0$, but in any case they allow us to determine each single μ_q in terms of μ_B. Therefore, each time we consider the case with $\Delta \neq 0$, we use the specific condition in eqs. (19) to express μ_q in eq. (8) in terms of μ_B.

Let us now discuss the main features of the hadron-quark phase transition, which we assume to be first-order, thus performing the Maxwell construction. Figure 1 shows numerical results for the pressure as a function of the

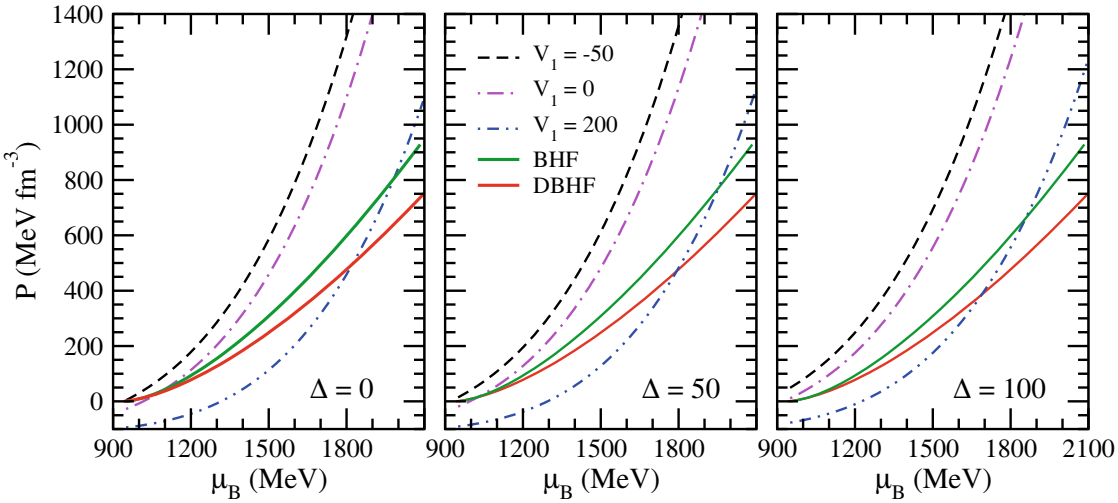

Fig. 1. (Color online) The pressure is displayed as a function of the baryon chemical potential μ_B for the FCM quark matter and the purely hadronic matter. All calculations for FCM have been performed for $G_2 = 0.006\,\mathrm{GeV}^4$, and several values of V_1 have been chosen. The solid curves represent the BHF (green) and DBHF (red) EoS. Each panel shows results for different values of the gap Δ, *i.e.* 0, 50, and 100 MeV.

baryon chemical potential μ_B in the hadronic matter and quark matter in beta equilibrium. In particular, the green (red) solid curves represent the BHF (DBHF) EoS, whereas the remaining curves are the results for the FCM model with different choices of the quark-antiquark potential V_1 (expressed in MeV). For completeness, a negative value of the potential, $V_1 = -50$ MeV is also included in this analysis. In the left, middle and right panels the value assumed for the gap Δ is respectively equal to 0, 50 and 100 MeV. All calculations shown in fig. 1 are performed taking $G_2 = 0.006\,\mathrm{GeV}^4$. We notice that with increasing the value of V_1 the transition point is shifted to larger values of the chemical potential, hence of the baryon density. However, the exact value depends also on the stiffness of the hadronic EoS at those densities. In this case, being the DBHF EoS stiffer than the BHF, the transition takes place at smaller values of the density. We notice that the transition point is affected also by the value of the gap Δ, and is shifted toward smaller μ_B for larger value of the gap. We also see that no phase transition occurs for negative values of V_1.

The resulting EoS, for the several cases discussed, is displayed in fig. 2, where one can directly read off the phase transition between hadron matter and quark matter under the Maxwell construction. We notice that the phase transition is allowed only for $V_1 \geq 0$, and that the width of the plateau is directly related to Δ. In the case $V_1 = 0$ (magenta curve) the phase transition takes place at very low value of the density, the plateau is quite small and the pure quark matter phase starts at density about 3 times normal nuclear matter density. By increasing V_1 the phase transition is shifted to larger values of the energy density.

4.2 Hybrid star structure

Once the EoS of the hybrid star matter is known, one can use the Tolman-Oppenheimer-Volkoff [75] equations for spherically symmetric NS:

$$\frac{\mathrm{d}p}{\mathrm{d}r} = -\frac{Gm\epsilon}{r^2}\frac{(1+p/\epsilon)(1+4\pi r^3 p/m)}{1-2Gm/r}\,, \tag{20}$$

$$\frac{\mathrm{d}m}{\mathrm{d}r} = 4\pi r^2 \epsilon, \tag{21}$$

where G is the gravitational constant and $m(r)$ is the enclosed mass within a radius r. Given a starting energy density ϵ_c, one integrates these equations until the surface $r = R$, and the gravitational mass is obtained by $M_G = m(R)$. The EoS needed to solve the TOV equations is taken from the neutron star matter calculations discussed above, and matched with the crust EoS, which has been taken from refs. [77].

As is well known, the mass of the NS has a maximum value as a function of radius (or central density), above which the star is unstable against collapse to a black hole. The value of the maximum mass depends on the EoS, so that the observation of a mass higher than the maximum mass allowed by a given EoS simply rules out that EoS. This is illustrated in fig. 3, where the relation between mass and radius (left panel) and central density (right panel) in units of the saturation density $\rho_0 = 0.17\,\mathrm{fm}^{-3}$ is displayed. Results are plotted for the case in which the BHF EoS is used for hadronic matter. In fig. 3 we plot several cases obtained for different values of V_1, G_2 and Δ and in this example the largest value of the maximum mass is observed for large values of $V_1 = 200$ MeV, $\Delta = 100$ and $G_2 = 0.01$, and it is compatible with the largest mass observed up to now, *i.e.* $(2.01 \pm 0.04)M_\odot$ in PSR J0348+0432 [3].

Recently, it has been shown in ref. [23] that the FCM equation of state can be accurately represented by the so-called CSS parameterization. The basic ansatz is that a sharp phase transition occurs to a high-density phase,

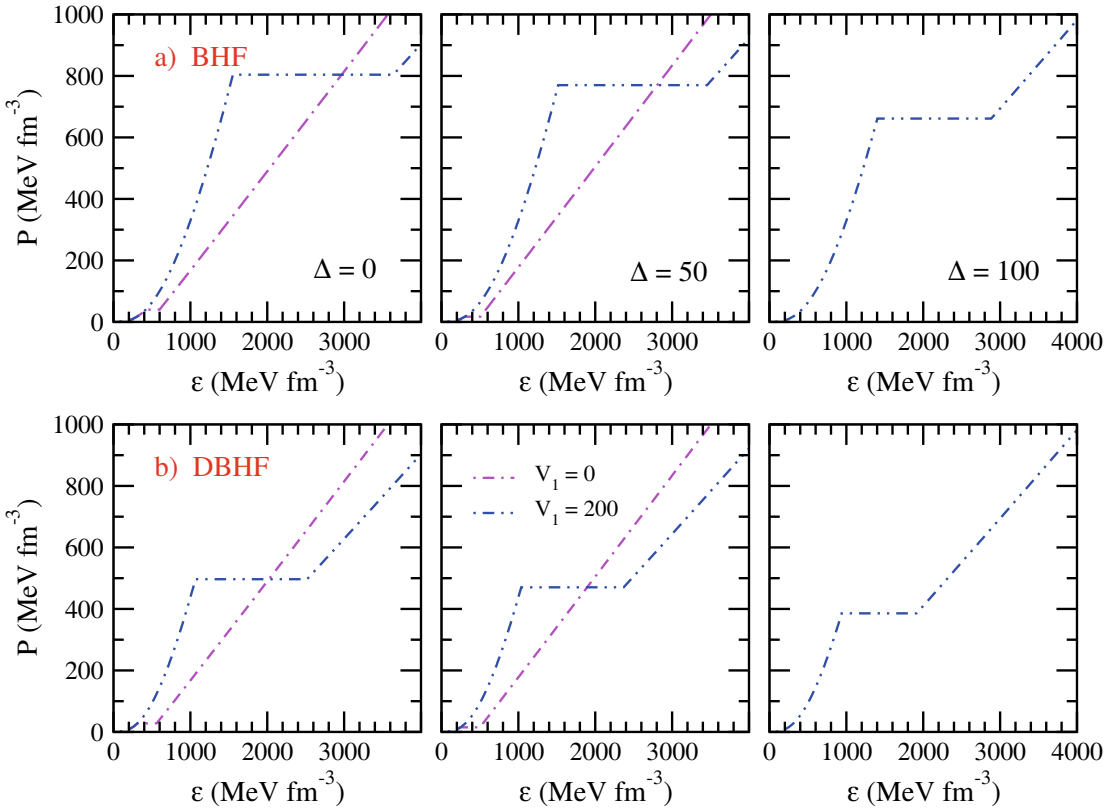

Fig. 2. (Color online) The pressure is displayed *vs.* the energy density for $V_1 = 0$ (magenta curves) and $V_1 = 200$ (violet) using as hadronic EoS the BHF (upper panels) and the DBHF (lower panels). All calculations for FCM have been performed for $G_2 = 0.006\,\mathrm{GeV}^4$. The left, middle and right panels correspond to the values $\Delta = 0, 50, 100\,\mathrm{MeV}$, respectively.

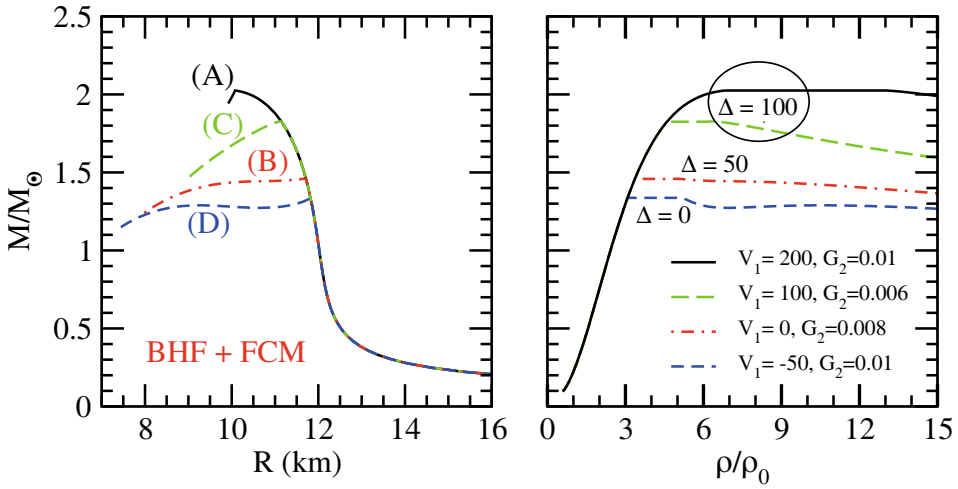

Fig. 3. (Color online) The mass as a function of the radius (left panel) and the central density (right panel) is displayed for several values of V_1, G_2 and Δ. The BHF EoS is used for the hadronic phase. The labels (A), (B), (C) and (D) indicate the specific topologies of the hybrid star branch.

where the speed of sound is density-independent. As already discussed in ref. [22], in all models of nuclear/quark matter one can find the four topologies of the mass-radius curve for compact stars: the hybrid branch may be connected to the nuclear branch (C), or disconnected (D), or both may be present (B) or neither (A). We will discuss in detail the FCM mapping onto the CSS parameterization in the next subsection. Here we limit ourselves to use

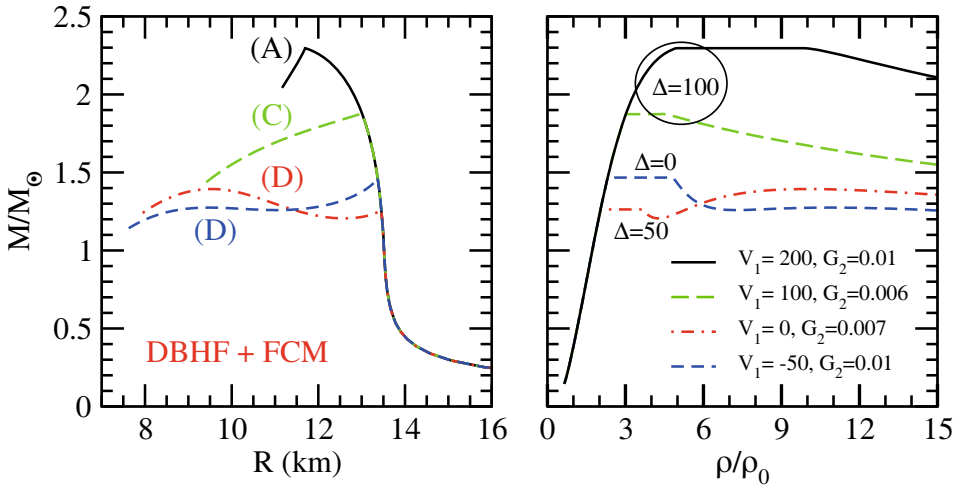

Fig. 4. Same as fig. 3, but for the DBHF EoS.

the same labels in figs. 3 and 4 in order to indicate the topology of the mass-radius curve, which is strongly related to the values of the pressure and energy density at the transition point, and to the energy density discontinuity. In the framework of the FCM model, the topology is related to the chosen values of V_1, G_2 and Δ. Using fig. 1 as a guide, we can obtain various topologies just changing V_1, G_2 and Δ. For example, when combining FCM quark matter to the BHF nuclear matter we find that, for unpaired quark matter and $V_1 = -50\,\mathrm{MeV}$, the lowest transition point can be obtained when $G_2 > 0.006\,\mathrm{GeV}^4$. In fig. 3 the corresponding mass-radius relation, obtained with $G_2 = 0.01\,\mathrm{GeV}^4$ is displayed by the blue dashed line, which exhibits a branch of stable hybrid stars disconnected (D) by the hadronic branch. With increasing V_1 the transition point moves to larger values of the pressure and the energy density, and as a consequence we explore regions of the phase diagram where the topology changes. For instance, for $V_1 = 0$ we can get both (B) connected and disconnected hybrid star branches, whereas for $V_1 = 100\,\mathrm{MeV}$ connected (C) hybrid star branches are present and, for the largest value of $V_1 = 200\,\mathrm{MeV}$ the hybrid branch is absent (A). This is clearly shown by a cusp in the mass-radius relation, and all configurations with radii smaller than the one characterizing the cusp are unstable. Therefore only purely nucleonic stars do exist in this case. However, the stability of those hybrid star configurations is related to the modeling of the deconfinement phase transition, as pointed out in ref. [78] where the Gibbs construction was used instead of the Maxwell method. The additional contribution of the CFL pressure to the FCM EoS produces only a shift of the transition point, and therefore the topology explored can be different than the one of the unpaired case, leaving unchanged the phase diagram.

In fig. 4 we display the mass-radius (left panel) and the mass-central density relation (right panel) in the case that the EoS used for the hadronic phase is the DBHF. We observe a topology similar to the one displayed in fig. 3, except the (B) configurations, which do not appear for the chosen set of values used for V_1, G_2 and Δ.

Finally we comment on the values of the maximum mass. In both cases, either BHF or DBHF EoS for the hadronic matter, we see that the largest possible values of the maximum mass are obtained only for values of $V_1 > 100\,\mathrm{MeV}$, and that only in the DBHF case maximum masses well above the observational limit are possible. In fact, the heaviest BHF+FCM hybrid star has a mass of $2.03 M_\odot$, and the heaviest DBHF+FCM hybrid star has a mass of $2.31 M_\odot$. Those values are indicated by an orange cross in fig. 5, where we display the mapping between the FCM and CSS parameters which are, in addition to the particular constant value of the speed of sound c_{QM}, the ratio of the pressure and energy density in nuclear matter at the transition point, $p_{\mathrm{trans}}/\epsilon_{\mathrm{trans}}$, and the ratio of the energy density discontinuity and the energy density at the transition, $\Delta\epsilon/\epsilon_{\mathrm{trans}}$. In the upper (lower) panels we show results for the BHF (DBHF) hadronic EoS, whereas in the left, middle and right panels calculations are reported for different values of the gap $\Delta = 0,\ 50,\ 100\,\mathrm{MeV}$, respectively. The solid red line shows the threshold value $\Delta\epsilon_{\mathrm{crit}}$ below which there is always a stable hybrid star branch connected to the neutron star branch. This critical value is given by [79–81]

$$\frac{\Delta\epsilon_{\mathrm{crit}}}{\epsilon_{\mathrm{trans}}} = \frac{1}{2} + \frac{3}{2}\frac{p_{\mathrm{trans}}}{\epsilon_{\mathrm{trans}}}\,, \tag{22}$$

and is obtained by performing an expansion in powers of the size of the core of the high-density phase. That result is analytical and independent on both c^2_{QM} and the hadronic EoS. The solid (dashed) green lines represent the phase boundaries for connected and disconnected branches, and are obtained for $c^2_{\mathrm{QM}} = 1/3(0.28)$. Those values span the range of c^2_{QM} relevant for the FCM, as discussed in [23].

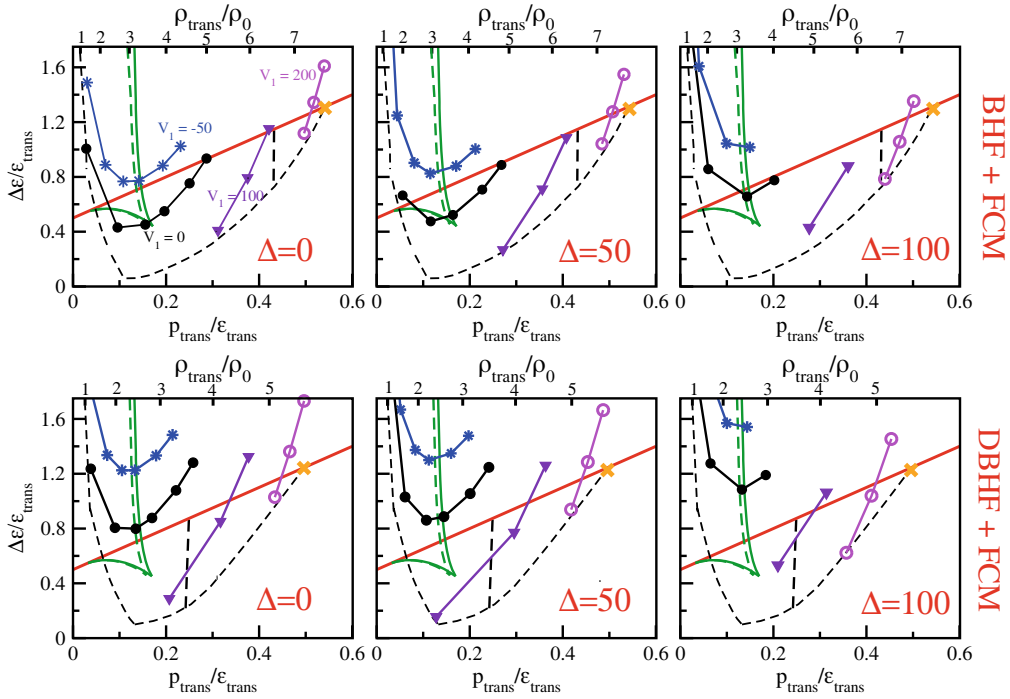

Fig. 5. The mapping of the FCM quark matter model onto the CSS parameterization. Results are obtained using the BHF (upper panels) and DBHF (lower panels) nuclear matter EoS. The green curves are the phase boundaries for the occurrence of connected and disconnected hybrid branches. The dashed black line delimit the region yielded by the FCM model. Within that region, the symbols give CSS parameter values for FCM quark matter as G_2 is varied at constant V_1 (given in MeV). The (orange) cross denotes the EoS with the highest $p_{\rm trans}$, which gives the heaviest FCM hybrid star. The left, middle, and right panels display results obtained with $\Delta = 0$, 50, and 100 MeV, respectively.

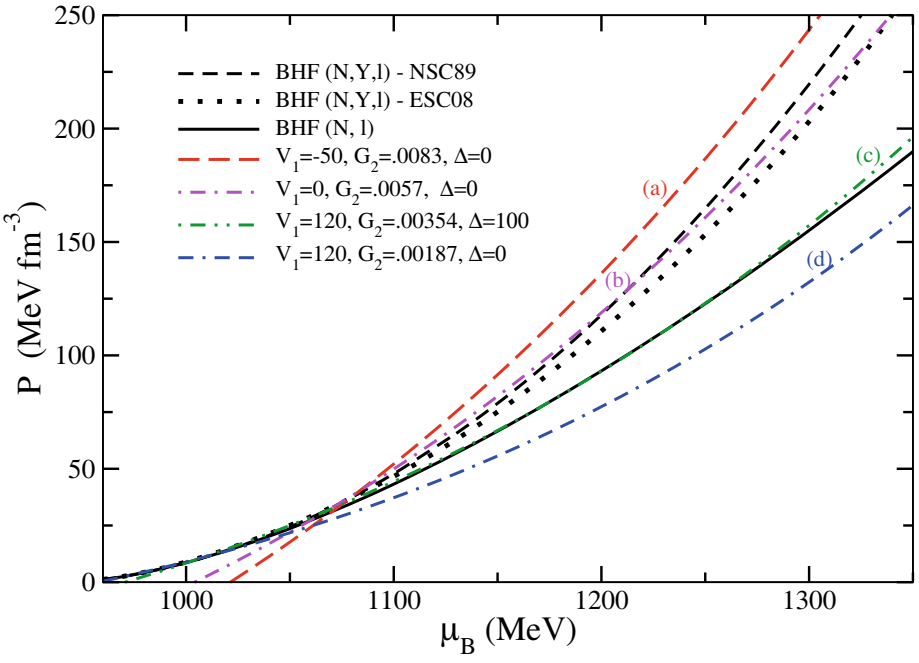

Fig. 6. Pressure *vs.* baryon chemical potential corresponding to the hadronic EoS's, including hyperons (dashed and dotted black lines) or without hyperons (BHF) (solid black line), and their crossing with the quark matter pressure evaluated with four different parameterisations ((a), (b), (c), (d) lines).

Table 1. The minimum and maximum values of G_2 (in units of GeV^4) are shown for different choices of Δ and V_1.

Δ (MeV)	V_1 (MeV)	$G_2^{\min}$	$G_2^{\max}$
0.	−50.	0.007	0.014
	0.	0.005	0.012
	100.	0.003	0.01
	200.	0.003	0.01
100.	−50.	0.009	0.014
	0.	0.007	0.012
	100.	0.006	0.01
	200.	0.003	0.01

Table 2. The total radius R, the radius of the quark core R_Q, the radius of the hadronic layer R_H and the crust radius R_{crust} are given for a hybrid star mass $M = 2M_\odot$, for different choices of the hadronic EoS and Δ. All radii are given in km.

EoS	Δ (MeV)	R	R_Q	R_H	R_{crust}
BHF	0.	10.37	0.055	9.97	0.345
	100.	10.44	0.215	9.87	0.355
DBHF	0.	12.78	1.27	10.87	0.640
	100.	12.72	2.42	9.665	0.635

The dashed black contour delimit the region accessible by the FCM calculation. Above that region, the symbols connected by solid lines show the CSS parameterization of the FCM quark matter EoS. Along each line we keep V_1 constant and vary G_2 over the range indicated in table 1 for the two extreme cases $\Delta = 0,\ 100\,\mathrm{MeV}$ and different values of V_1, for both BHF and DBHF. In fig. 5 V_1 varies from $-50\,\mathrm{MeV}$ up to the maximum value at which hybrid star configurations occur, which is indicated by an (orange) cross. For the BHF case that value is $V_1 = 240\,\mathrm{MeV}$, $G_2 = 0.0024\,\mathrm{GeV}^4$ and for the DBHF case it is $V_1 = 255\,\mathrm{MeV}$, $G_2 = 0.0019\,\mathrm{GeV}^4$. The vertical black dashed lines indicate the parameter regions accessible by the FCM and consistent with the measurement of a $M = 2M_\odot$. Hybrid stars with mass heavier than $2M_\odot$ lie on a very small connected branch on the right side of the vertical black dashed lines, and cover a small range of central pressures, having a very tiny quark core, with mass and radius similar to those of the heaviest purely hadronic star, as was already discussed in ref. [23]. For completeness, we display in table 2 the characteristic radius of a hybrid star with $M = 2M_\odot$ obtained with BHF and DBHF EoS for the hadronic phase and two extreme values for $\Delta = 0,\ 100\,\mathrm{MeV}$. We chose typical configurations lying on the vertical black lines plotted in fig. 5. We notice that the radius of the quark core R_Q is bigger for the stiffest hadronic EoS, being comprised between 1 and 3 km, whereas for the soft hadronic EoS the quark core radius R_Q is not larger that a few hundreds meters. In both cases the hadronic layer occupies the largest portion of the star, and is characterized by a radius R_H of about 10 km. The crust radius R_{crust} is always smaller than 1 km.

Moreover we notice in fig. 5 that along each line of constant V_1, $p_{\mathrm{trans}}/\epsilon_{\mathrm{trans}}$ grows with G_2, and this can be explained by recalling the linear dependence of the quark pressure on G_2 in eq. (10), so that, at fixed chemical potential, an increase of G_2 lowers the quark pressure, making quark matter less favourable, and shifting the transition point to higher chemical potential or pressure. This was already discussed in ref. [20] for BHF nuclear matter, and is equally applicable to DBHF nuclear matter. We also see in fig. 5 that the combination of G_2 and V_1 moves the curves inside the region accessible by FCM which is delimited downward by the dashed black line. Figure 5 shows that the introduction of a color-flavor locking effect characterized by a gap Δ does not change qualitatively the gross features of the phase transition, being the topology of the hybrid star branch slightly affected.

4.3 Effects of hyperons on the phase transition

It is known that the effect of including hyperons in the hadronic EoS is to soften the interior of the NS so that it becomes difficult to get masses of the stars as heavy as 2 solar masses. In our analysis, this is confirmed by the pressure obtained for the two parameterizations NSC89 and ESC08, which are plotted in fig. 6 (respectively, dashed and dotted black curves) together with the BHF EoS (solid black curve) used in sect. 4.1. In fact, the steeper growth with μ_B of the former two curves with respect to the latter is an indication of the greater stiffness of the EoS when hyperons are neglected. At the same time we notice that the NSC89 and ESC08 parameterizations quantitatively give very close results. We stress that in this paper we discuss hyperon effects obtained only in the BHF approach.

Then, it is easy to realise that the inclusion of hyperons puts more stringent constraints on the parameters of the quark matter EoS, in order to observe a crossing of the pressures in the two phases. In fig. 6 we report four examples of quark matter pressure for different choices of the parameters (curves (a), (b), (c), (d)). These curves explicitly show that the parameter V_1 is mainly responsible for their slope, while Δ has a much smaller effect and G_2, being an additive constant to the pressure as shown in eq. (10), produces a global upward or downward shift of the quark matter pressure.

Therefore, when going from $V_1 = -50\,\mathrm{MeV}$ to $V_1 = 0$ to $V_1 = 120\,\mathrm{MeV}$, the corresponding curves (a), (b) and (c) become less and less steep, and one can observe three representative behaviors: (a) shows a phase transition at a crossing point below 1100 MeV with any hadronic EoS; (b) has the same crossing as in the case (a) and, when compared to the BHF EoS, it remains the favoured phase at any μ_B, but when compared to the NSC89 or ESC08 parameterizations, one observes a second crossing at larger μ_B; (c), after an interval in which the pressures for the hadronic and quark phases are substantially the same, the NSC89 or ESC08 curves stay above (c) which, in turn is above the BHF curve.

Therefore, one learns that the quark pressure can exceed the pressure of hadronic EoS including hyperons only

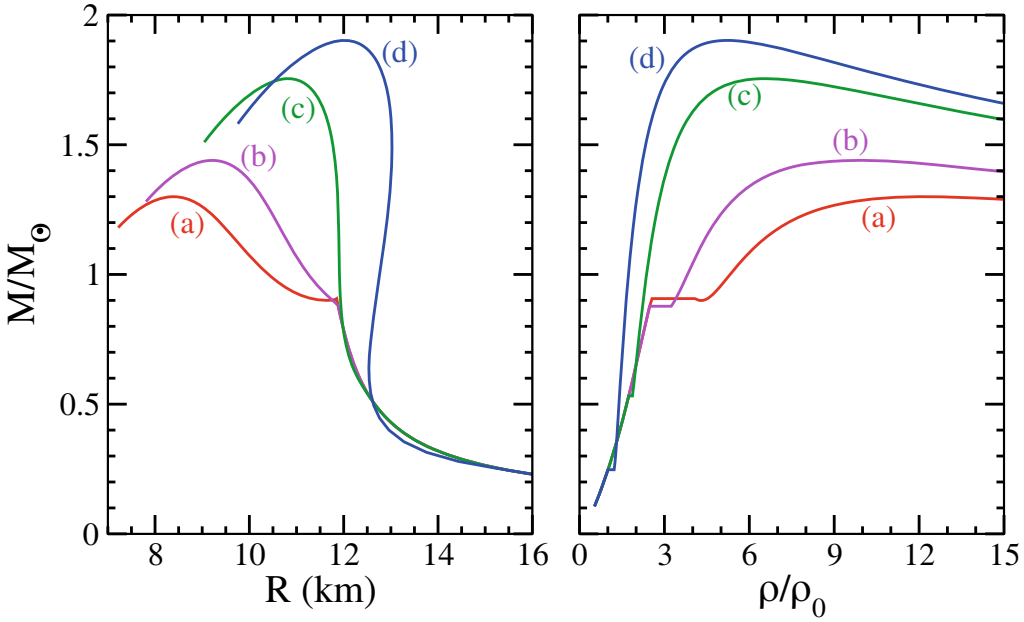

Fig. 7. Mass-radius (left panel) and mass-central density (right panel) plots of the hybrid stars corresponding to the quark matter EoS (a), (b), (c), (d) together with the hyperon parameterization ESC08 of fig. 6.

at small V_1, typically well below 100 MeV, and one knows from the analysis of sect. 4.2 that smaller V_1 correspond to NS with smaller masses. To verify this point, we consider the cases (a) and (b) (retaining for (b) only the first crossing of the quark and hadronic pressure) and then derive the corresponding mass-radius or mass-central density relation which are given in fig. 7 for the ESC08 EoS (the NSC89 case produces almost indistinguishable results). It is evident that in the cases (a) and (b), the masses remain below $1.5M_\odot$. In addition, for (b) we ignored the second crossing point above which, in principle, the hadronic phase becomes again favourable, but, in any case, this new transition would make the NS even softer thus lowering its maximum mass and ruling out the possibility of reaching $2M_\odot$.

Before concluding, we reconsider in the other cases the procedure followed for (b), namely the derivation of the mass-radius relation obtained by systematically considering only the transition from hadronic to quark matter occurring at the lowest value of μ_B, while ignoring other potential transitions occurring at higher μ_B.

By following this procedure, which is somehow justified by our poor knowledge of the hyperon interactions, we reconsider in detail the various examples of fig. 6 and, for convenience, we report in fig. 8 an enlargement of the region at small μ_B. In fact, from fig. 8 it is evident that the double transition which is observed at a larger scale in fig. 6 for the case (b), now occurs on a smaller scale for the cases (c) and (d). These two examples are realized with $V_1 = 120$ MeV and, respectively, $\Delta = 100$ MeV and $\Delta = 0$ and G_2 is tuned to make the quark matter pressure almost tangent to the NSC89 or ESC08. While the case (c) crosses for the first time the hadronic EoS's slightly above $\mu_B \sim 1000$ MeV, where the ESC08 and the BHF EoS's are distinguishable, the crossing of curve (d) occurs below $\mu_B \sim 980$ MeV, before the onset of hyperons.

In both cases (c) and (d), the second crossing is very close, but according to the assumption made we retain only the quark matter EoS at larger μ_B after the first crossing. The interesting point is that, as $V_1 = 120$ MeV is rather large for these two cases, one expects large maximum masses for the corresponding NS. This can be verified by looking at the right panel of fig. 7, where after a very small plateau, related to the small difference between the quark and hadronic pressure along a rather large interval around the transition point, the mass of the NS grows above $1.7M_\odot$ for (c) and up to $1.95M_\odot$ for (d) that is reasonably close to the observational constraint of $2M_\odot$. It is remarkable that very similar results are obtained for the maximum NS masses in [82] where the NSC89 parameterization is used for hyperons and a sort of QCD corrected bag model for quark matter.

5 Conclusions

The FCM extension at finite T and μ_B provides us a very simple description of the quark dynamics in terms of two parameters, namely the gluon condensate G_2, that parametrizes the vacuum pressure and energy density, and hence is strictly related to the bag constant of the MIT bag model, and the potential V_1, which summarizes the interaction corrections to the free quark and gluon pressure. It is then natural to explore the predictions of the FCM on the maximum masses (and their associated radii) of NS when these parameters are varied. In order to have a more complete picture, we include the effect of color superconductivity through the CFL mechanism, which amounts to the addition of a new free energy contribution written in terms of the gap Δ.

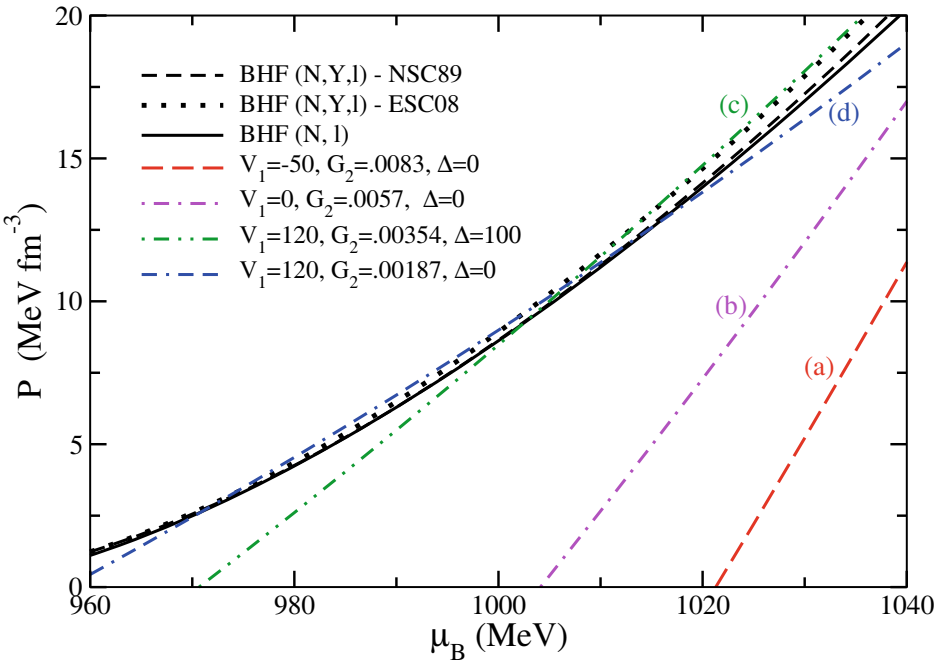

Fig. 8. Enlargement of the low μ_B region of fig. 6.

Clearly, any prediction of a quark matter model on the structure of a hybrid NS strongly depends on the nuclear matter EoS employed and among the large variety of nuclear EoS available in the literature, we focused on the nonrelativistic BHF EoS and its relativistic counterpart, the DBHF EoS. These are derived within a solid microscopic approach, and give us different predictions on the NS maximum mass. For completeness, we also analyzed the inclusion of the hyperon degrees of freedom that produces a softening of the nuclear matter EoS with the consequent reduction of the maximum mass of the NS.

With this new set of more refined calculations, we confirm the trend already observed in [20, 21, 23], *i.e.* the maximum mass of hybrid stars grows with the two parameters V_1 and G_2 while it decreases when Δ is increased. More interestingly, we extend the mapping developed in [23] among the parameters of the FCM and those defining the CSS parameterization, by displaying the effect of the gap Δ. In fact, from the various panels of fig. 5, it is evident that the border of the area of the diagram accessible by the FCM (*i.e.* the dashed black curve) is not sensitive to Δ and it is totally determined in terms of the CSS parameters. In particular, even the region corresponding to configurations associated to hybrid stars with maximum mass greater than $2M_\odot$, which is the triangle-like area delimited above by the straight solid red line, below by the dashed black curve and finally on the left by the almost vertical dashed black segment, is only determined in terms of the two CSS parameters reported on the x and y axes of the diagrams. Therefore one can conclude that a particular configuration with mass around or above two solar masses can be realized in the FCM by different pairs of G_2 and V_1, depending on the specific value assigned to Δ, *i.e.* the appearance of a color superconducting gap can be mimicked by a shift of the other two parameters. Therefore, even the mass of the heaviest hybrid star predicted by the FCM (the orange crosses in fig. 5) does not correspond to a unique set of G_2, V_1 and Δ, while, as seen in [23], its value strongly depends on the specific choice made for the nuclear matter EoS.

The inclusion of the hyperons induces dramatic changes in this picture. In fact, a regular transition from nuclear to quark matter with a stable quark phase up to very high chemical potential requires a particular tuning of the FCM parameters that leads to very low maximum masses, below $1.5M_\odot$. We have also observed that it is possible to find specific sets of the parameters G_2, V_1 and Δ such that the hadronic and quark matter pressure run very close for a large range of μ_B and, when looking more in detail, one observes multiple crossings of these lines, although at large μ_B the phase that includes hyperons is favoured. For completeness we analyze these cases by retaining only the first crossing from the hadronic to the quark matter phase, and neglecting the other transitions at higher chemical potential. In this case it is possible to tune the FCM parameters in such a way to raise the maximum mass up to $1.95M_\odot$, although an explanation supporting the strong assumption on the transition is required in order to accept this result.

We thank H.-J. Schulze (INFN, Sezione di Catania) for providing us with the BHF EoS for hypernuclear matter with the NSC89 and ESC08 nucleon-hyperon parameterizations. We are also grateful to M. Alford for bringing the CSS parameterization to our attention. Partial support comes from "NewCompStar", COST Action MP1304.

References

1. N.K. Glendenning, *Compact Stars: Nuclear Physics, Particle Physics, and General Relativity*, 2nd edition (Springer-Verlag New York, 2000).
2. P.B. Demorest, T. Pennucci, S.M. Ransom, M.S.E. Roberts, J.W.T. Hessels, Nature **467**, 1081 (2010) arXiv:1010.5788.
3. J. Antoniadis, P. Freire, N. Wex, T. Tauris, R. Lynch *et al.*, Science **340**, 1233232 (2013) arXiv:1304.6875.
4. M. Baldo, I. Bombaci, G. Burgio, Astron. Astrophys. **328**, 274 (1997) astro-ph/9707277.
5. A. Akmal, V.R. Pandharipande, D.G. Ravenhall, Phys. Rev. C **58**, 1804 (1998) nucl-th/9804027.
6. X.R. Zhou, G.F. Burgio, U. Lombardo, H.-J. Schulze, W. Zuo, Phys. Rev. C **69**, 018801 (2004).
7. M. Baldo, A. Polls, A. Rios, H.-J. Schulze, I. Vidaña, Phys. Rev. C **86**, 064001 (2012) arXiv:1207.6314.
8. Z. Li, U. Lombardo, H.-J. Schulze, W. Zuo, Phys. Rev. C **77**, 034316 (2008).
9. P. de Forcrand, PoS **LAT2009**, 010 (2009).
10. Y. Aoki, G. Endrődi, Z. Fodor, S.D. Katz, K.K. Szabó, Nature **443**, 675 (2006) hep-lat/0611014.
11. A. Bazavov, T. Bhattacharya, M. Cheng, N.H. Christ, C. Detar, S. Ejiri, S. Gottlieb, R. Gupta, U.M. Heller, K. Huebner, C. Jung, F. Karsch, E. Laermann, L. Levkova, C. Miao, R.D. Mawhinney, P. Petreczky, C. Schmidt, R.A. Soltz, W. Soeldner, R. Sugar, D. Toussaint, P. Vranas, Phys. Rev. D **80**, 014504 (2009) arXiv:0903.4379.
12. G.F. Burgio, M. Baldo, P.K. Sahu, H.-J. Schulze, Phys. Rev. C **66**, 025802 (2002) nucl-th/0206009.
13. M. Baldo, M. Buballa, G.F. Burgio, F. Neumann, M. Oertel, H.-J. Schulze, Phys. Lett. B **562**, 153 (2003) nucl-th/0212096.
14. C. Maieron, M. Baldo, G.F. Burgio, H.-J. Schulze, Phys. Rev. D **70**, 043010 (2004) nucl-th/0404089.
15. M. Baldo, G.F. Burgio, P. Castorina, S. Plumari, D. Zappala, Phys. Rev. C **75**, 035804 (2007) hep-ph/0607343.
16. H. Chen, M. Baldo, G.F. Burgio, H.-J. Schulze, Phys. Rev. D **84**, 105023 (2011) arXiv:1107.2497.
17. H.G. Dosch, Phys. Lett. B **190**, 177 (1987).
18. H.G. Dosch, Y. Simonov, Phys. Lett. B **205**, 339 (1988).
19. Y. Simonov, Nucl. Phys. B **307**, 512 (1988).
20. M. Baldo, G. Burgio, P. Castorina, S. Plumari, D. Zappala, Phys. Rev. D **78**, 063009 (2008) arXiv:0804.2328.
21. S. Plumari, G. Burgio, V. Greco, D. Zappala, Phys. Rev. D **88**, 083005 (2013) arXiv:1307.3055.
22. M.G. Alford, S. Han, M. Prakash, Phys. Rev. D **88**, 083013 (2013) arXiv:1302.4732.
23. M.G. Alford, G.F. Burgio, S. Han, G. Taranto, D. Zappalà, Phys. Rev. D **92**, 083002 (2015) arXiv:1501.0790.
24. M. Baldo (Editor), *Nuclear Methods and The Nuclear Equation of State* (World Scientific, Singapore, 1999).
25. T. Gross-Boelting, C. Fuchs, A. Faessler, Nucl. Phys. A **648**, 105 (1999) nucl-th/9810071.
26. H. Song, M. Baldo, G. Giansiracusa, U. Lombardo, Phys. Rev. Lett. **81**, 1584 (1998).
27. M. Baldo, A. Fiasconaro, H.Q. Song, G. Giansiracusa, U. Lombardo, Phys. Rev. C **65**, 017303 (2002).
28. B. Day, Phys. Rev. C **24**, 1203 (1981).
29. A. Lovato, O. Benhar, S. Fantoni, A.Y. Illarionov, K.E. Schmidt, Phys. Rev. C **83**, 054003 (2011) arXiv:1011.3784.
30. J. Carlson, V. Pandharipande, R.B. Wiringa, Nucl. Phys. A **401**, 59 (1983).
31. R. Schiavilla, V. Pandharipande, R.B. Wiringa, Nucl. Phys. A **449**, 219 (1986).
32. Z. Li, H. Schulze, Phys. Rev. C **85**, 064002 (2012).
33. A. Lovato, O. Benhar, S. Fantoni, K.E. Schmidt, Phys. Rev. C **85**, 024003 (2012) arXiv:1109.5489.
34. D. Logoteta, I. Vidaña, I. Bombaci, A. Kievsky, Phys. Rev. C **91**, 064001 (2015) arXiv:1502.0124.
35. S.A. Coon, H.K. Han, Few-Body Syst. **30**, 131 (2001) nucl-th/0101003.
36. E. Epelbaum, A. Nogga, W. Glöckle, H. Kamada, U.-G. Meißner, H. Witała, Phys. Rev. C **66**, 064001 (2002) nucl-th/0208023.
37. P. Navrátil, Few-Body Syst. **41**, 117 (2007) arXiv:0707.4680.
38. M. Baldo, K. Fukukawa, Phys. Rev. Lett. **113**, 242501 (2014) arXiv:1409.7206.
39. K. Fukukawa, M. Baldo, G.F. Burgio, L. Lo Monaco, H.-J. Schulze, arXiv:1507.0728.
40. Y. Fujiwara, K. Fukukawa, Few-Body Syst. **54**, 2357 (2013).
41. M. Baldo, G. Burgio, H. Schulze, Phys. Rev. C **58**, 3688 (1998).
42. M. Baldo, G. Burgio, H. Schulze, Phys. Rev. C **61**, 055801 (2000) nucl-th/9912066.
43. P.M.M. Maessen, T.A. Rijken, J.J. de Swart, Phys. Rev. C **40**, 2226 (1989).
44. V.G.J. Stoks, T.A. Rijken, Phys. Rev. C **59**, 3009 (1999) nucl-th/9901028.
45. H.-J. Schulze, T. Rijken, Phys. Rev. C **84**, 035801 (2011).
46. J. Haidenbauer, Nucl. Phys. A **914**, 220 (2013) *International Conference on Hypernuclear and Strange Particle Physics (HYP2012)*.
47. J. Haidenbauer, S. Petschauer, N. Kaiser, U.-G. Meißner, A. Nogga, W. Weise, Nucl. Phys. A **915**, 24 (2013).
48. D. Lonardoni, F. Pederiva, S. Gandolfi, Phys. Rev. C **89**, 014314 (2014).
49. I. Vidaña, D. Logoteta, C. Providencia, A. Polls, I. Bombaci, EPL **94**, 11002 (2011) arXiv:1006.5660.
50. D. Logoteta, I. Vidaña, C. Providencia, Nucl. Phys. A **914**, 433 (2013) *International Conference on Hypernuclear and Strange Particle Physics (HYP2012)*.
51. Y. Yamamoto, T. Furumoto, N. Yasutake, T.A. Rijken, arXiv:1510.0609.
52. G. Brown, W. Weise, G. Baym, J. Speth, Commun. Nucl. Part. Phys. **17**, 39 (1987).
53. M. Baldo, G. Giansiracusa, U. Lombardo, I. Bombaci, L.S. Ferreira, Nucl. Phys. A **583**, 599 (1995).
54. Z.H. Li, U. Lombardo, H.-J. Schulze, W. Zuo, L.W. Chen, H.R. Ma, Phys. Rev. C **74**, 047304 (2006).
55. T. Katayama, K. Saito, Phys. Lett. B **747**, 43 (2015) arXiv:1501.0541.
56. A. Di Giacomo, H.G. Dosch, V. Shevchenko, Y. Simonov, Phys. Rep. **372**, 319 (2002) hep-ph/0007223.
57. Y. Simonov, M. Trusov, JETP Lett. **85**, 598 (2007) hep-ph/0703228.
58. Y. Simonov, M. Trusov, Phys. Lett. B **650**, 36 (2007) hep-ph/0703277.
59. A. Nefediev, Y. Simonov, M. Trusov, Int. J. Mod. Phys. E **18**, 549 (2009) arXiv:0902.0125.

60. M.A. Shifman, A. Vainshtein, V.I. Zakharov, Nucl. Phys. B **147**, 385 (1979).
61. M.A. Shifman, A. Vainshtein, V.I. Zakharov, Nucl. Phys. B **147**, 448 (1979).
62. M. D'Elia, A. Di Giacomo, E. Meggiolaro, Phys. Lett. B **408**, 315 (1997) hep-lat/9705032.
63. M. D'Elia, A. Di Giacomo, E. Meggiolaro, Phys. Rev. D **67**, 114504 (2003) hep-lat/0205018.
64. I. Bombaci, D. Logoteta, Mon. Not. R. Astron. Soc. Lett. **433**, L79 (2013) arXiv:1212.5907.
65. T.D. Cohen, R. Furnstahl, D.K. Griegel, Phys. Rev. C **45**, 1881 (1992).
66. E. Drukarev, M. Ryskin, V. Sadovnikova, Prog. Part. Nucl. Phys. **47**, 73 (2001) nucl-th/0106049.
67. M. Baldo, P. Castorina, D. Zappala, Nucl. Phys. A **743**, 3 (2004) nucl-th/0311038.
68. M.A. Metlitski, A.R. Zhitnitsky, Nucl. Phys. B **731**, 309 (2005) hep-ph/0508004.
69. A. Zhitnitsky, AIP Conf. Proc. **892**, 518 (2007) hep-ph/0701065.
70. M.G. Alford, K. Rajagopal, F. Wilczek, Nucl. Phys. B **537**, 443 (1999) hep-ph/9804403.
71. M.G. Alford, A. Schmitt, K. Rajagopal, T. Schfer, Rev. Mod. Phys. **80**, 1455 (2008) arXiv:0709.4635.
72. K. Rajagopal, F. Wilczek, Phys. Rev. Lett. **86**, 3492 (2001) hep-ph/0012039.
73. M. Alford, K. Rajagopal, JHEP **06**, 031 (2002) hep-ph/0204001.
74. M. Alford, M. Braby, M. Paris, S. Reddy, Astrophys. J. **629**, 969 (2005) nucl-th/0411016.
75. S.L. Shapiro, S.A. Teukolsky, *Black Holes, White Dwarfs and Neutron Stars: The Physics of Compact Objects* (Wiley-VCH, 1986).
76. I. Bombaci, U. Lombardo, Phys. Rev. C **44**, 1892 (1991).
77. J.W. Negele, D. Vautherin, Nucl. Phys. A **207**, 298 (1973).
78. D. Logoteta, I. Bombaci, Phys. Rev. D **88**, 063001 (2013) arXiv:1309.0096.
79. R. Schaeffer, L. Zdunik, P. Haensel, Astron. Astrophys. **126**, 121 (1983).
80. Z.F. Seidov, Sov. Astron. **15**, 347 (1971).
81. L. Lindblom, Phys. Rev. D **58**, 024008 (1998) gr-qc/9802072.
82. A. Kurkela, P. Romatschke, A. Vuorinen, Phys. Rev. D **81**, 105021 (2010) arXiv:0912.1856.